# Colloidal sol of UO2 nanoparticles supported by multi-lamellar vesicles of carboxylate based surfactant

Zijie Lu, Joseph Lautru, Thomas Zemb, Diane Rébiscoul

# Colloidal sol of $UO_2$ nanoparticles supported by multi-lamellar vesicles of carboxylate based surfactant

*Zijie Lu*[1], *Joseph Lautru*[1], *Thomas Zemb*[1], *Diane Rébiscoul*[1]

[1] Institut de Chimie Séparative de Marcoule, CEA, UMR 5257 CEA-CNRS-UM-ENSCM, 30207 Bagnols-sur-Cèze, France.

KEYWORDS: Colloidal Sol-gel, $UO_2$ nanoparticle, multi-lamellar vesicle, carboxylate surfactants.

## Abstract

Producing compact monoliths of mesoporous uranium oxide that are free from surface active components and able to be wet by highly radioactive solutions is of great interest for future nuclear technologies. In this direction, metastable colloidal sols of $UO_2$ using U(IV) as precursor and carboxylic surfactants (Polyoxyethylene(9) oleyl ether carboxylic acid $C_{16/18:1}E_9COOH$ and Polyoxyethylene(10) lauryl ether carboxylic acid $C_{12}E_{10}COOH$) have been successfully prepared by indirect precipitation for $6 \leq pH \leq 8$ with a molar ratio between uranium and surfactant $U/S < 0.3$. The self-assembly of this colloidal system results in micelles and U(IV) species partitioned as different forms: U-$C_{16/18:1}E_9COOH$/U-$C_{12}E_{10}COOH$ complexes forming multi-lamellar vesicles with interdigitated bilayers, $UO_2$ nanocrystallites (nc-$UO_2$) within the vesicles and nc-$UO_2$ forming aggregates attached on the surface of the vesicles with a relative proportion of 61%:28%:11%. We showed that using an amphiphilic molecule having carboxylic head group,

U(IV) species can be complexed and form multi-lamellar vesicles as supporting gel. The competition between the U(IV) species complexation by surfactant molecules and their hydrolysis prevents the rapid condensation of $U(OH)_{4-n}^{n+}(1\leq n\leq 4)$ and makes the colloidal sol-gel process controllable. The principle shown here that results in partitioning the uranium into molecules, nanoparticles and aggregates could be useful in the design of molecularly dispersed Uranium and Plutonium coming from sol-gel chemistry.

# 1. INTRODUCTION

Nuclear fuel preparation for future generations of nuclear reactor is a challenging task regarding the safety conditions. Generally, fuels such as $UO_x$ ($UO_2$)[1-3], $ThO_2$[3, 4] and $MO_x$ ($UO_2$-$PuO_2$ mixed oxides[5-8]) fuels are synthesized by powder metallurgical routes[9]. Such preparation presents several disadvantages such as potential contamination problem due to $UO_2$ microparticles powder and also for MOx preparation[10] where the ultimate mixing of U/Pu has to be homogenous at a nanoscale. Low temperature chemical processes in aqueous solution such as colloidal sol-gel process leading to the possible formation of an organized mesoporosity in actinides oxides matrix, may be a real interesting alternative for several reasons[11-14]. First, from a safety point of view, the aqueous colloidal sol-gel route avoids dried powder manipulation by operators and the formation of hotspot due to the repulsions of actinides oxides particles in solution in the case of $UO_2$/$PuO_2$ mixture. Second, the presence of organized mesoporosity in the $UO_2$ final material provides advantages such as (i) the possibility of an homogenous $PuO_2$ incorporation into the mesopores avoiding hotspot formation, (ii) the fission gas release during the fuel burning in

nuclear reactor through the porous network if the pores are connected and, (iii) due to its high specific surface area, the increase of its dissolution rate during its reprocessing[15, 16]. Third, the homogeneity and the ultimate morphology of such materials can be easily adjusted to fit with different types of nuclear reactor.

Since early 1960s, several colloidal sol-gel routes (Internal[17, 18] and External Gelation Process[19], Total Gelation Process[20] and Complex Sol-Gel Process[21]) have been developed for the synthesis of oxides or mixed oxides of actinides (Uranium, Thorium, Plutonium…). These kinds of process yield actinide oxides microspheres. However, there is a lack of investigation regarding the preparation of mesostructured actinide materials. Recently, Zhao et al. reported the synthesis of ordered mesoporous uranium dioxide via a complex multi-step "nanocasting" route[22]. Using ordered mesoporous silicates as hard templates, the authors have successfully synthesized $UO_2$ powder having a rod-like morphology at nanoscale. Nevertheless, to our best knowledge, no study of the colloidal sol-gel route coupled with soft template molecules with a view to synthetize actinide oxides presenting organized porosity has been reported. This is the goal of this study focusing on the understanding of the sols to, one day, be able to prepare highly organized $UO_2$ materials.

Indeed, after the discovery of ordered mesoporous silica in 1990s, the synthesis of mesoporous material has been largely extended to other non-siliceous elements such as transition metals, rare earth elements, etc.[23-25]. Generally, two types of sol-gel processes are used based on different forms of precursors: the polymeric route using alkoxides and the colloidal route using metal salts. Nevertheless, the synthesis of actinides alkoxides is

fastidious due to the high reactivity of these species and thus, difficult to control from an industrial point of view[26, 27]. Therefore, the colloidal route using metal salts presents an interesting alternative.

In the colloidal sol-gel route using metal salts, the main difficulty is the control of the reactivity, i.e the relative kinetics of nucleation, growth and coagulation of the colloids and their condensation leading to the network formation around the templating agent. Nucleation and growth must be balanced, while coagulation in the form of microparticles must be avoided[28]. Depending on the metal salt, the pH has to be controlled and the addition of a complexing agent can be required.[29] Recently with U(IV) solution at 6<pH<8, Leblanc and al.[30] have used carboxylate surfactants with a non-ionic polyethoxylated part between its anionic group and its hydrophobic alkyl chains as complexing and templating agent for the preparation of structured mesoporous $UO_2$ materials. The final $UO_2$ materials synthesized from stable sols of $UO_2$ nanocrystallites was only partially lamellar structured as observed by Transmission Electron Microscopy.

Based on the same colloidal system, we have intended to better control the processes driving the formation of this lamellar structure and the distributions of uranium species in the sol. Thus, we have studied thoroughly the distribution of U(IV) species in the sols and the competition between the $UO_2$ formation and the complexation of soluble uranium species by the carboxylate group of the surfactants. To reach this goal, the surfactant solutions and the sols prepared by indirect precipitation from U(IV) solution were characterized by Small and Wide Angle X-ray Scattering (SWAXS), and Infrared Spectroscopy (IR).

## 2. MATERIALS AND METHODS

**2.1 Materials.** AKYPO RO 90 VG (Polyoxyethylene(9) oleyl ether carboxylic acid, $C_{16/18:1}E_9COOH$, Mw = 722 g $mol^{-1}$) and AKYPO RLM 100 (Polyoxyethylene(10) lauryl ether carboxylic acid, $C_{12}E_{10}COOH$, Mw = 685 g $mol^{-1}$) from Kao Chemicals were used as received.

**2.2 Surfactant solutions preparation.** $C_{16/18:1}E_9COOH$ and $C_{12}E_{10}COOH$ were dissolved in Mili-Q water to prepare solutions at $10^{-1}$ M and referred as $C_{16/18}E_9$ and $C_{12}E_{10}$. This concentration is higher than the critical micellar concentration ($10^{-4}$ M)[31] and the surfactants form an isotropic micellar phase. The pH of the surfactant solutions were adjusted from an initially $pH_{20°C}$=2.3 to 6, 7, 8 and 9 by adding a 3 M $NH_4OH$ solution. At these pH values the carboxylic groups of surfactant molecules are deprotonated (apparent pKa value is around 5.3 ± 0.2 at $10^{-1}$ M[32]) and the precipitation of $UO_2$(am) is favorable since its saturation index is positive and constant when the pH value is higher than 5[33]. The prepared surfactant solutions were then stocked in the dark to avoid solution alteration until their analyses [30].

**2.3 U(IV) solution preparation.** Uranium chloride solution (U(IV) solution) was prepared by dissolution of uranium metal in 6 M HCl solution. The uranium metal chips were firstly washed in 2 M HCl to dissolve the oxide impurities then rinsed with water and ethanol. Finally, the pretreated uranium metal was dissolved in 6 M HCl to prevent the oxidation of uranium and maintain uranium at the oxidation state IV for several months[34]. Based on the titration method presented in Dacheux et al.[35], the uranium concentration of U(IV) solution

was 0.515 ± 0.002 M.

**2.4 Preparation of colloidal dispersions.** Uranium sols were prepared by indirect precipitation[33] in the glove box under nitrogen to keep the oxygen concentration under 1 ppm. First, the surfactant solutions were degassed to remove dissolved oxygen. Then U(IV) solution was added dropwise into 8 mL of surfactant solution until the target concentration of U(IV) was reached. After each drop addition, the pH value of the colloidal dispersions was corrected by adding a degassed solution of 3 M $NH_4OH$. Table 1 presents the references, the final pH and the molar ratio between uranium and surfactant U/S.

**Table 1** References, final pH and molar ratio U/S of the colloidal dispersions.

| Reference | pH | U/S | Reference | pH | U/S |
|---|---|---|---|---|---|
| $C_{16/18}E_9$-6-0.16 | 5.9 | 0.16 | $C_{12}E_{10}$-6-0.13 | 6.0 | 0.13 |
| $C_{16/18}E_9$-6-0.18 | 6.0 | 0.18 | $C_{12}E_{10}$-6-0.21 | 6.2 | 0.21 |
| $C_{16/18}E_9$-6-0.25 | 6.0 | 0.25 | $C_{12}E_{10}$-6-0.3 | 5.9 | 0.3 |
| $C_{16/18}E_9$-6-0.33 | 6.1 | 0.33 | $C_{12}E_{10}$-7-0.13 | 6.8 | 0.13 |
| $C_{16/18}E_9$-6-0.5 | 5.9 | 0.5 | $C_{12}E_{10}$-7-0.21 | 7.1 | 0.21 |
| $C_{16/18}E_9$-7-0.16 | 7.0 | 0.16 | $C_{12}E_{10}$-8-0.13 | 8.0 | 0.13 |
| $C_{16/18}E_9$-7-0.18 | 7.0 | 0.18 | | | |
| $C_{16/18}E_9$-7-0.25 | 7.4 | 0.25 | | | |
| $C_{16/18}E_9$-8-0.16 | 8.0 | 0.16 | | | |
| $C_{16/18}E_9$-8-0.18 | 7.9 | 0.18 | | | |
| $C_{16/18}E_9$-8-0.25 | 7.9 | 0.25 | | | |
| $C_{16/18}E_9$-9-0.16 | 8.8 | 0.16 | | | |

| | | | |
|---|---|---|---|
| $C_{16/18}E_9$-9-0.18 | 9.1 | 0.18 | |
| $C_{16/18}E_9$-9-0.25 | 9.1 | 0.25 | |

**2.5 Characterization.** Solutions were analyzed using Fourier Transformed Infrared spectroscopy (FTIR) with a Perkin Elmer Spectrum 100 spectrometer in Attenuated Total Reflection (ATR) mode equipped with a DTGS/KBR detector. The samples were placed at the surface of the diamond. The spectra were recorded from 400 to 4000 $cm^{-1}$ adding 32 scans with a 2 $cm^{-1}$ of resolution correcting from the background spectrum for each substrate. Baseline adjustments were performed using the Origin software. Small and Wide Angle X-ray Scattering (SWAXS) analysis were carried out in transmission geometry with a Xenocs setup equipped with a Mo anode ($\lambda$ = 0.71 Å) using a MAR345 2D imaging plate detector. Such short wavelength allows the probing of a scattering range from few angstroms to 30 nm and at the same time, is only weakly absorbed by the high-z elements such as uranium. The collimation was ensured by a Fox2D multilayer mirror and by a set of scatterless slits that delimitated the beam to a square section (0.8 mm side length at the sample position). The distance from the sample to the detector was about 750 mm and was calibrated using silver behenate powder. Sols were analyzed in glass capillaries of 2 mm of diameter. Azimuthal averaging of 2D-data recorded by a MAR345 imaging plate detector was performed using the FIT2D software taking into account the electronic background of the detector, the empty cell subtraction and an intensity calibration. The scattered intensity in absolute scale (in $cm^{-1}$) was expressed versus the magnitude of the scattering vector $q = (4\pi\sin\theta)/\lambda$, where $\theta$ was the scattering angle. Experimental resolution was $\Delta q/q = 0.02$. An Environmental Scanning Electron Microscope (ESEM) FEI Quanta 200 FEG with a Scanning Transmission Electronic

Microscope (STEM) stage is used to observe the vesicles. This stage is composed by a TEM grid holder fixed above a STEM detector, which is composed of two segments for Bright Field (BF) and Dark Field (DF) imaging. Indeed, this device allows getting an image with the transmitted electron in order to improve the resolution. After the vesicles deposition on TEM grid, the sample was mounted on the stage in the microscope chamber. Then the micrographs are done under $10^{-3}$Pa vacuum. The conditions for imaging are a high voltage between 10kV and 20kV, a working distance between 4mm and 6mm and a magnification between X10000 and X100000. Low resolution Transmission electron microscopy (TEM) analyses were conducted at 200 kV on a Jeol200CX TEM equipped with a Photonic-Science camera.

## 3. RESULTS AND DISCUSSION

### 3.1 pH sensitivity of surfactant solutions

Surfactant solutions were characterized using ATR-FTIR. The results of $C_{16/18}E_9$ and $C_{12}E_{10}$ (Figure SI1 (a) and (b) respectively) do not show any significant modification as a function of pH except on the C-O-C stretching band of ether backbone of $C_{16/18}E_9$ samples. Indeed, the C-O-C stretching band (around 1070 $cm^{-1}$) presents a slight increase of the absorbance.

In order to determine the impact of pH on the self-assembly of the surfactant and their structure in the surfactant solutions, SWAXS analysis have been carried out. Figure SI2 presents the SWAXS patterns of different surfactant solutions at different pH. Whatever the surfactant, the variation of pH from 2.3 to 9 has no distinguishable impact either on the size

of micelles or on their globular structure. This low pH sensitivity is different than the behavior of fatty acid solutions which a slight pH variation leads to a phase transition (an example is given in Figure SI3 with octanoic acid).

The results obtained from the fitting of the experimental SWAXS patterns at pH comprised between 6 and 9, show core-shell micelles having a radius of 3.2 nm and a number of aggregation $\approx$ 100 for the $C_{16/18}E_9$ and 2.9 nm and $\approx$ 90 for the $C_{12}E_{10}$ (see Figures SI4, Tables SI1 and SI2.). The decrease of forward intensity is mainly due to the electrostatic repulsion linked to the deprotonation of core-shell micelles modifying the intermolecular interaction.

### 3.2 Stability of the colloidal dispersions

We have systematically varied pH and U(IV) to surfactant molar ratio U/S using the one pot method described previously. After the addition of U(IV) solution and the pH adjustment, the stability of the colloidal dispersion was noted. When the dispersion was unstable, the precipitation was observed few hours after the addition of U(IV) solution. The colloidal dispersion with $C_{16/18}E_9$ remained stable for more than 1 month and the colloidal dispersion with $C_{12}E_{10}$ started to precipitate after 1 week. Since these two dispersions remained stable for a relative long time even in presence of heavy elements, they could be therefore considered as sols and were referred to $C_{16/18}E_9$ sols and $C_{12}E_{10}$ sols. A few hours after the stirring, the changes of color from green to dark brown for $C_{16/18}E_9$ sols and clear brown for $C_{12}E_{10}$ sols were observed indicating the formation of $UO_2$ nanoparticles. Figure 1 presents the domain of solution stability prepared with (a) $C_{16/18}E_9$ and (b) $C_{12}E_{10}$ as a function of the

pH and the molar ratio U/S. The results show that whatever the surfactant, the solutions are stable for pH comprised between 6 and 8. $C_{16/18}E_9$ sols were obtained for 0.1 < U/S < 0.3 and $C_{12}E_{10}$ sols for 0.1 < U/S < 0.25.

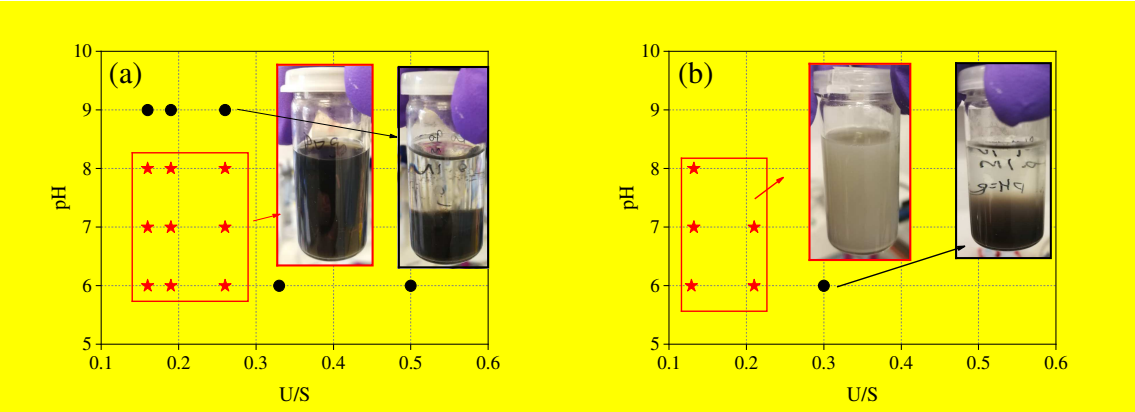


**Figure 1.** Stability ranges of pH and molar ratio U/S for colloidal dispersions prepared with (a) $C_{16/18}E_9$ and (b) $C_{12}E_{10}$ (red stars represent sols and black spheres represent unstable dispersions).

### 3.3 Structure of the sols at colloidal scale

In order to determine the modification of phase structure after the addition of U(IV) solution, SWAXS analysis was carried out. The SWAXS patterns of sols are presented on the Figure 2 and reveal that the structuration of these two types of sols are close.

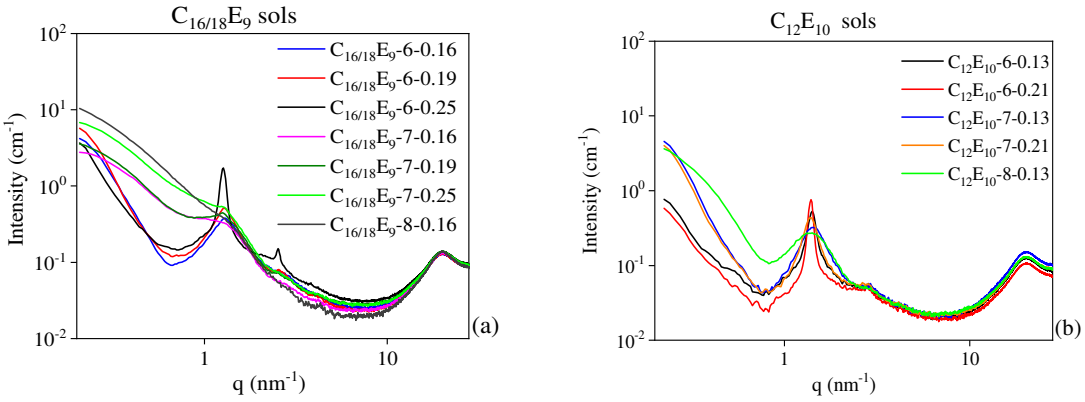


**Figure 2.** SWAXS patterns of the sols of (a) $C_{16/18}E_9$ and (b) $C_{12}E_{10}$.

The medium chain $C_{12}$ and the long chain $C_{18}$ have similar but not identical behaviors. The common point is liquid ordered structure producing the Lorentzian broad peak at q=20 $nm^{-1}$. In the intermediate q range, a lamellar structure is detected with two first orders of reflection. In the case of long chains, we observe disordered locally lamellar structures producing no second order except for the sample $C_{16/18}E_9$-6-0.25 producing rigid lamellar structure ($L_\beta$). In the following part, we focus on the $C_{16/18}E_9$ sols which shows the best stability through the study of the effect of the pH and the U/S ratio on the self-assembly of the surfactant and their structure within the sols.

### 3.3.1 Effect of pH

The Figure 3 (a) presents the SWAXS patterns of the $C_{16/18}E_9$ sols at different pH with a molar ratio U/S=0.25.

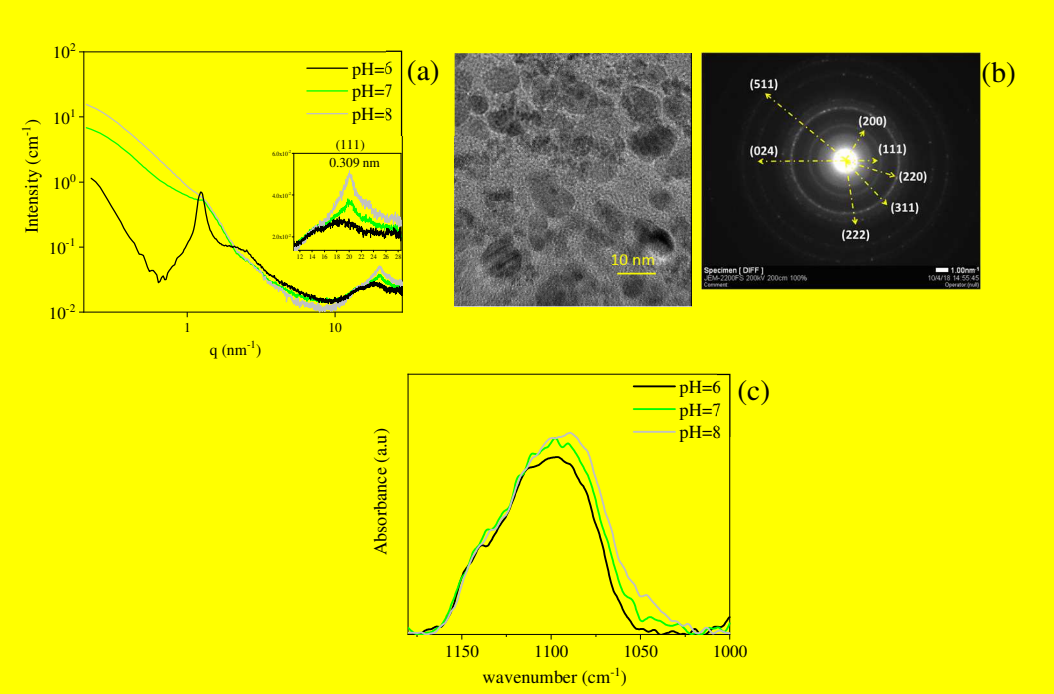


**Figure 3.** (a) SWAXS patterns of $C_{16/18}E_9$ sols with a molar ratio U/S=0.25 at different pH. The SWAXS pattern of water was subtracted to the sols one; (b) TEM image and electron diffraction pattern of $UO_2$ aggregates from $C_{16/18}E_9$-8-0.25 sol; (c) FTIR spectra focus on the C-O-C stretching band of sols with a molar ratio U/S=0.25 at different pH.

After the addition of the U(IV) solution, two main modifications which depend on the pH and which are characteristic of the presence of $UO_2$ nanoparticles and/or aggregates of $UO_2$ are visible on the SWAXS patterns. First, the large peak growing at 20 $nm^{-1}$ is associated with the crystalline plane (111) of a fluorite-type structure of $UO_2$ nanocrystallites (nc-$UO_2$) [30, 36-38]. This peak becomes more intense with the pH increase. Indeed, the increase of pH favors the formation of nc-$UO_2$ and bigger aggregates of nc-$UO_2$. The formation of objects having a size bigger than 20 nm is suggested by the increase of the signal at low q compared to the one of surfactant solutions. All of these results are attested by the TEM image of the sol $C_{16/18}E_9$-8-0.25 presented on Figure 3 (b) showing the presence of aggregates of nanocrystallites around ten nanometers having a size comprised between 3 nm and 12 nm. Moreover the electron diffraction pattern of several nanoparticles (Figure 3 (b)) displays the (111), (200), (220), (222), (311), (024) and (511) planes of a face-center-cubic lattice. This is

confirmed by the SWAXS pattern showing a large peak at high q (insert figure in Figure 3 (a)) where the maximum corresponds to a distance of 0.309 nm. This is in agreement with the interplanar distance between crystallographic planes of the (111) face-center-cubic lattice of $UO_2$ (0.3153 nm, 00-041-1422 ICDD[39]).

Second, as already observed in[30], a bilayer-based $L_\alpha$ phase is present in $C_{16/18}E_9$-6-0.25 sols. The addition of U(IV) solution has changed a part or all the initial core-shell structure existing in the surfactant solution to a $L_\alpha$ structure having 4.8 nm of repeating distance. The high electronic density of U(IV) complexed by $C_{16/18}E_9COOH$ surfactants leads to a decrease of the head area occupied by each surfactant ($a_0$). This induces an increase of the spontaneous packing parameter: $P_0(U/S)=\frac{V}{a_0(U/S)l}$ where l is the average chain length and V is the molecular volume. Unlike classical surfactant system, the area $a_0$ and therefore the spontaneous packing parameter $P_0$ are now a function critically controlled by the uranium to surfactant U/S. In other words, the $L_\alpha$ is promoted when $P_0$ is near 1. Moreover, the repeating distance is smaller than the length of the average alkyl chain of one $C_{16/18}E_9$ molecule, which is about 6 nm according the Tanford's equation[40]. Even though taking into account that the alkyl chains are not fully extended, this is incompatible with the periodicity of the lamellar phase $L_\alpha$ obtained in this study. Therefore, the alkyl chains of $C_{16/18}E_9$ molecule must be at least partially interdigitated with another $C_{16/18}E_9$ molecule and form the bilayers. Such interdigitation of alkyl chains can be observed on the bilayers of lipids with two alkyl chains[41-43]. However, some single-chained surfactants having a sufficiently large headgroup area could also form an interdigitated thin bilayer[44]. Indeed, close contacts between the charged headgroups are unfavorable. The alkyl chains are forced

to interdigitated in order to keep the neighboring headgroups apart. Similar phenomena have been observed with dialkyldimethylammonium Bromides bilayers[45-47]. In addition, the increase of the sol pH ($C_{16/18}E_9$-7-0.25 and $C_{16/18}E_9$-8-0.25 sols) leads to a strong attenuation of the peaks attributed to this lamellar structure. This could be explained by the increase of the amount of nc-$UO_2$ and bigger aggregates of nc-$UO_2$ at higher pH which decreased the concentration of complexed $U(OH)_n^{4-n}$ ($n < 4$) species and probably the concentration of lamellar structures.

All of these results deduced from SWAXS are supported by the FTIR analysis on the C-O-C stretching $\nu_{C\text{-}O\text{-}C}$ of the ether backbone at 1090 $cm^{-1}$ (Figure 3 (c)). Along the increase of pH, a broadening of $\nu_{C\text{-}O\text{-}C}$ peak to 1050 $cm^{-1}$ is observed. This variation could be due to two reasons: (i) the variation of C-O-C stretching along with the change of pH as observed in Figure SI1(a); (ii) the increase of pH causes an aggregation of nc-$UO_2$ attaching to the ether backbone which slows down the vibrations.

In conclusion, the increase of pH benefits the formation of nc-$UO_2$ and their aggregation. This phenomenon causes a partial deformation of the $L_\alpha$ structure. Thus, $C_{16/18}E_9$-6-0.25 being the sol presents the most organized lamellar-like structure, it has been chosen to determine the effect of the U/S ratio.

### 3.3.2 Effect of U/S ratio on sols U

Figure 4 (a) presents the SWAXS patterns of the sols with U/S molar ratio from 0.16 to 0.25. With the increase of U/S ratio, the two first orders of the $L_\alpha$ microstructure become more intense and thinner. This reveals an increase of the amount of lamellar phase as well as

a decrease of the fluctuation of the interlayer distance. Indeed, the rise of U(IV) species concentration in the media leads to the increase of the U(IV) species complexation by the surfactant and thus, the transformation of globular micelle to an $L_\alpha$ phase presented as multi-layered vesicles (MLV). The STEM image of $C_{16/18}E_9$-6-0.25 shown in Figure 4 (b) confirmed the existence of vesicles in the colloidal system. In addition, compared with the study of the pH effect (Figure 3 (a)), no significant change is observed in the high q region with the increase of U/S ratio. This attests that the complexation of U(IV) species is a preferential mode compared to the nc-$UO_2$ precipitation.

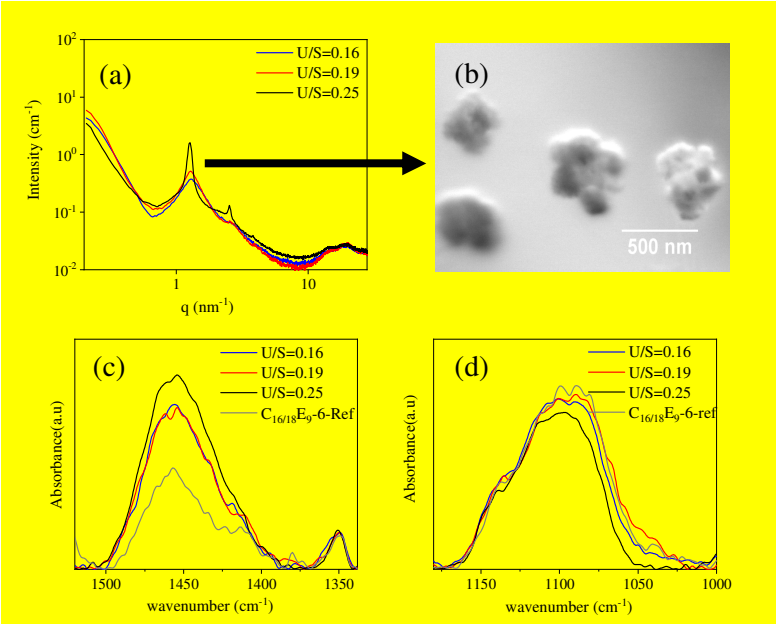


**Figure 4.** (a) SWAXS curves of sols U with different U/S ratios at pH=6 (The SWAXS pattern of water was subtracted to the sols one); (b) STEM image of the vesicles presented in $C_{16/18}E_9$-6-0.25; (c) FTIR spectra of stable sols U at pH=6 with different U/S ratio focus on the C-H (a) and C-O-C and (d) stretching bands. $C_{16/18}E_9$-6-Ref is referred to 0.1 M $C_{16/18}E_9$ surfactant solution at pH=6.

Apart from the change of structuration of sols showing by SWAXS analysis, FTIR spectra of these samples present also some modifications with the U/S ratio. Figure 4 (c) shows that peak of the C-H stretching bonds increases with U/S ratio probably due to the phase transformation from globular micelles to multi-lamellar vesicles. Such modification of

C-H bands have been already associated to a phase transformation[48]. In addition, Figure 4 (d) shows that the C-O-C stretching band around 1080 $cm^{-1}$ presents a decrease of the contribution of the vibration at low wave number leading to a decrease of the peak width with a higher U/S ratio. Dehydration of ether backbone due to the interdigitation of hydrophobic chain of the surfactant may be responsible for this peak modification[48].

### 3.4 Qualitative and quantitative analyses of sol $C_{16/18}E_9$-6-0.25

In order to have a clear description of the components (U(IV) species, nc-$UO_2$, surfactant) distribution and of the system organization, the sol $C_{16/18}E_9$-6-0.25 was centrifuged at 14000 rpm until the obtaining of clear supernatant (S) and a dense gel (G). The SWAXS patterns of the two phases after separation are presented on the Figure 5 (a).

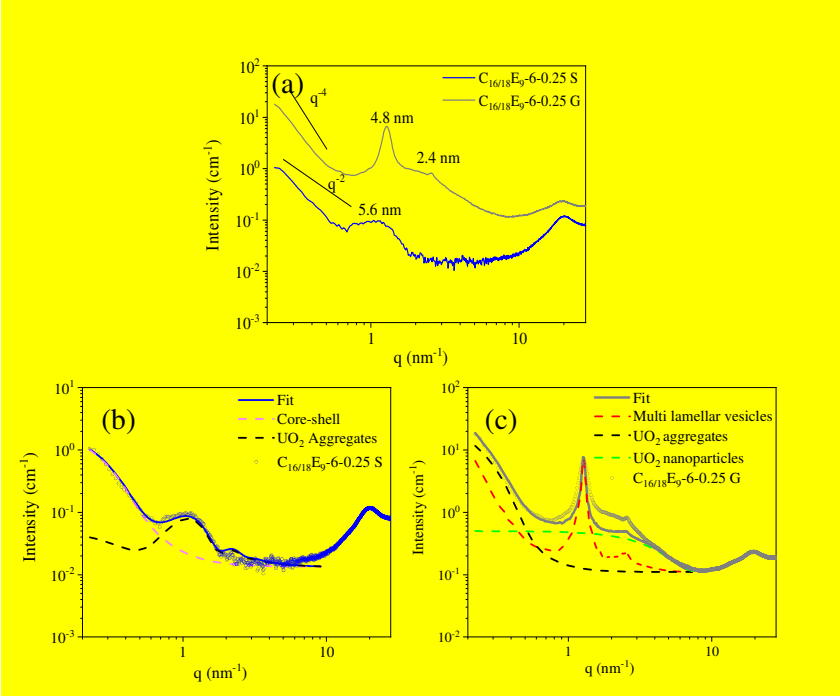


**Figure 5.** (a) SWAXS patterns of the supernatants $C_{16/18}E_9$-6-0.25 S and the dense gel $C_{16/18}E_9$-6-0.25 G of the sample $C_{16/18}E_9$-6-0.25; (b) Experimental and simulated SWAXS patterns of $C_{16/18}E_9$-6-0.25 S; (c) Experimental and simulated SWAXS patterns of $C_{16/18}E_9$-6-0.25 G.

The SWAXS patterns show that both, the supernatants and the dense gel present the two same microstructure observed previously (Figure SI2 and Figure 2), i.e. a micellar phase and a $L_\alpha$ phase in multi-lamellar vesicles respectively. Besides, the pattern of $C_{16/18}E_9$-6-0.25 S presents the same core-shell structure as for the surfactant solution but with an increase of the intensity of the scattering signal in the small q region with a slope close to $q^{-2}$. This may be due to the presence of nc-$UO_2$ aggregates in the supernatant.

To refine quantitative results, the SWAXS patterns of $C_{16/18}E_9$-6-0.25 S and $C_{16/18}E_9$-6-0.25 G were simulated on absolute scale. First, for the simulation of the experimental SWAXS pattern of $C_{16/18}E_9$-6-0.25 S, we have taken into account two contributions: (i) a fraction of core-shell micelles having the electron density of the $C_{16/18}E_9$ surfactants and (ii) a fraction of dispersed aggregates of nanoparticles with an exponential mass fractal model[49]. The fitting parameters and the simulated SWAXS patterns corresponding to the best fit are presented on the Table SI3 and Figure 5 (b) respectively.

Consequently, the supernatant of the $C_{16/18}E_9$-6-0.25 mainly consists of $UO_2$ aggregates and core-shell micelles of $C_{16/18}E_9$ surfactants. From this simulation, the fraction of surfactant complexing U(IV) species was calculated. Indeed, knowing the number density of core-shell micelles existing in the initial $C_{16/18}E_9$ solution from the simulation presented in Table SI2, and the number density of core-shell micelles in the $C_{16/18}E_9$-6-0.25 S, we can deduce that 21% of $C_{16/18}E_9$ surfactant molecules are still present as globular micelles and 79% of them are complexed by U(IV) species. Moreover, by interpreting the forward scattering $I_0$, the fraction of $UO_2$ aggregates was determined and count for about 1 % of the total U(IV) species (see

supporting information Table SI2 and section D).

Now, the full q range experimental SWAXS pattern of $C_{16/18}E_9$-6-0.25 G can be safely simulated by combining three contributions: (i) a fraction of vesicles having a multi-lamellar structure and the density of the $C_{16/18}E_9$ surfactant; (ii) a fraction of spherical nanoparticles having the density of $UO_2$; (iii) a fraction of dispersed aggregates of nanoparticles with an exponential mass fractal model[49]. The fitting parameters and the simulated SWAXS pattern corresponding to the best fit are presented in Table SI4 and Figure 5 (c) respectively.

The contributions of the multi-lamellar vesicles, core-shell micelle and of aggregates used in the simulated SWAXS patterns are also presented. The fitting results allowing the acquisition of a density of spherical nc-$UO_2$ (see Table SI3). Hence, we can deduce that about 28% of U(IV) species has formed nc-$UO_2$. Furthermore, these nc-$UO_2$ are also present inside the multi-lamellar vesicles. That is why they can be separated from the supernatant $C_{16/18}E_9$-6-0.25 S during the centrifugation. In fact, the competition between hydrolysis-condensation of uranium species and the complexation U(IV) and surfactants leads to the liberation of U(IV) species in solution allowing the formation of nc-$UO_2$. In addition, by interpreting the forward scattering intensity of the aggregates fraction in the fitting data (see Tables SI2 and SI3), we deduce that about 10% of U(IV) species has formed $UO_2$ aggregates with a gyration radius around 7.5 nm. The calculations are presented in supporting information (section D). Furthermore, it is possible that the aggregates present in $C_{16/18}E_9$-6-0.25 are attached on the surface of the vesicles. That is why they are present in the $C_{16/18}E_9$-6-0.25 S after centrifugation. Moreover, the size and the morphology of the vesicles were determined by analyzing one drop of $C_{16/18}E_9$-6-0.25 by STEM. The image is presented

on the Figure 4 (b). The image reveals that some vesicles having a size of around 200 nm are stuck together. As proposed previously, this may be due to the presence of $UO_2$ aggregates at the surface of the vesicles linking the vesicles between each other.

As so far, we are able to determine the distributions of U(IV) species as well as $C_{16/18:1}E_9COOH$ molecules partitioned as different forms in the system U-$C_{16/18:1}E_9COOH$ (see Table 2).

**Table 2.** Distributions of U(IV) species and $C_{16/18:1}E_9COOH$ molecules in the system of $C_{16/18}E_9$-6-0.25.

| Components | Forms | Portions |
|---|---|---|
| U(IV) species | U-$C_{16/18:1}E_9COOH$ MLV | 61% |
| | nc-$UO_2$ | 28% |
| | $UO_2$ aggregates | 11% |
| $C_{16/18:1}E_9COOH$ molecules | U-$C_{16/18:1}E_9COOH$ MLV | 79% |
| | Globular micelles | 21% |

### 3.6 Multi-scale structure of the final system

The multi-scale structure of the system is presented on Figure 7 and shows a schematic overview of the solution–sol transition of the $C_{16/18}E_9$-6-0.25 at different scales.

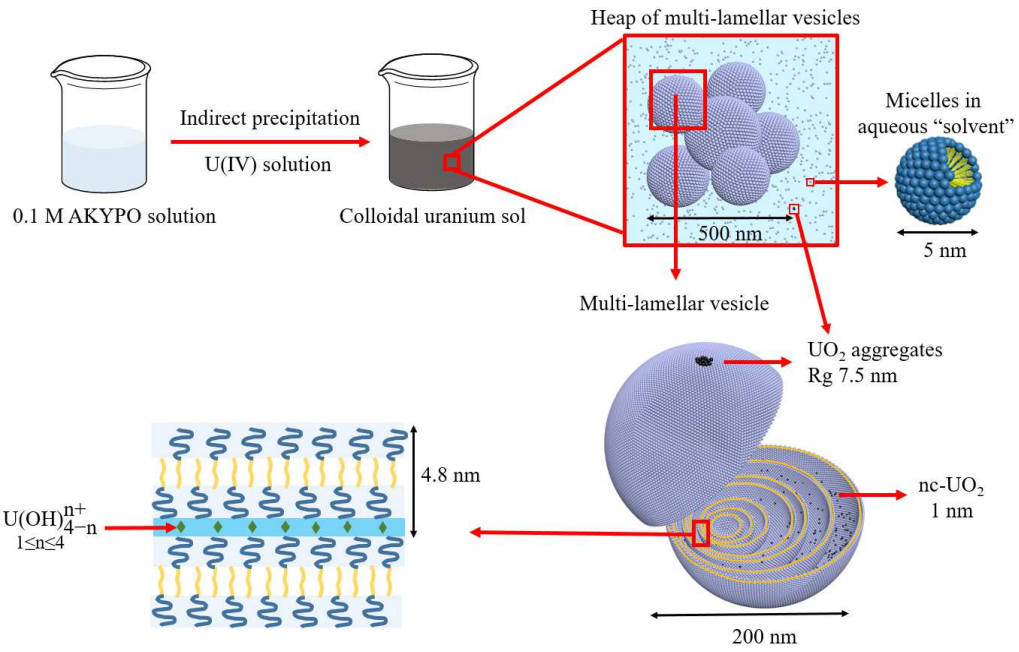


**Figure 7.** Schema of U-$C_{16/18:1}E_9COOH$ system.

Added to an $C_{16/18}E_9$ solution at 0.1 M presenting core-shell micelles, U(IV) solution leads to the formation of an homogeneous dark green colloidal uranium sol. The complexation of $U(OH)_{4-n}^{n+}(1\leq n\leq 4)$ by deprotonated carboxylic function of $C_{16/18}E_9$ molecules induced the shape transformation of a part of micelles (79 %) to multi-lamellar vesicles having around 200 nm size (See Figure 13) having interdigitated alkyl chains. Thus, 21% of $C_{16/18}E_9$ surfactant having no interaction with uranium species as counter-ions remains as micelles. In addition, during the indirect precipitation process, 11% of U(IV) species precipitate in the form of nc-$UO_2$ forming aggregates adsorbed on the surface of the vesicles. These $UO_2$ aggregates may act as nodes from one vesicle to another leading to the formation of heaps. Around 28% of U(IV) species form nc-$UO_2$ with a size about 1 nm are also present within the vesicles. The small size of these nanocrystallites may be due to: (i) the limited concentration of free U(IV) species ($U(OH)_{4-n}^{n+}(1\leq n\leq 4)$) which directly precipitate to form nc-$UO_2$ at the equilibrium with the U(IV) species complexed by $C_{16/18}E_9$ surfactants or/and (ii)

the limited amount of U(IV) species in the volume between the surfactant layers estimated to be an order of magnitude of -19 in mole.

Figure 8 presents the distribution of U(IV) species as a function of the different forms in U- $C_{16/18:1}E_9COOH$ system.

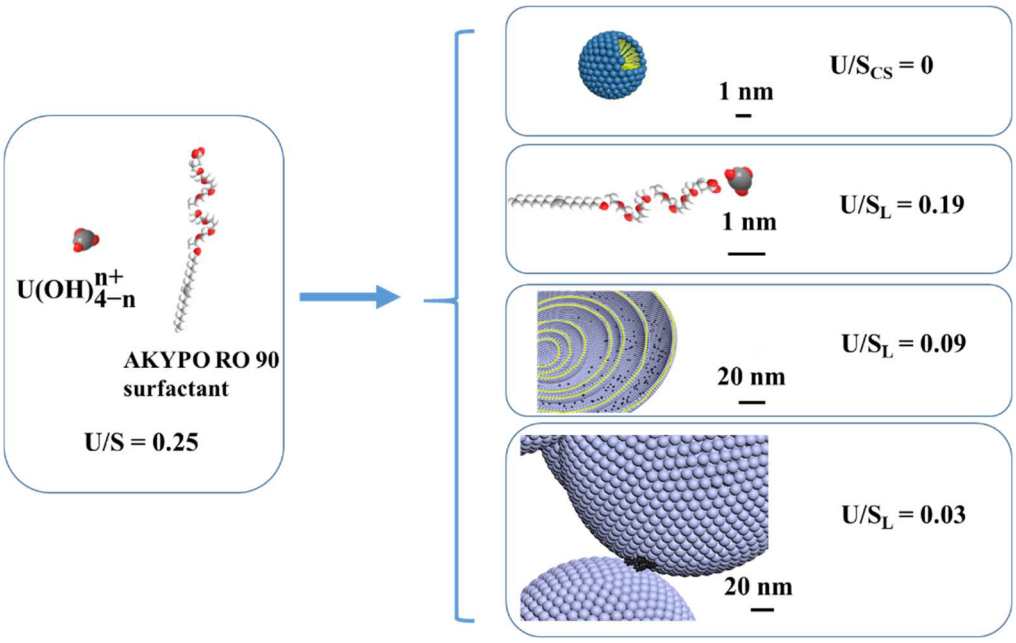


**Figure 8.** Distribution U(IV) species in the system. $S_{CS}$ is referred to surfactants forming core-shell micelles; $S_L$ is referred to surfactants forming multi-lamellar vesicles.

As we mentioned before, during the indirect precipitation, there is a competition between the complexation of U(IV) species by $OH^-$ (1) and the complexation of U(IV) by the carboxylate group of surfactant molecules (2).

$$U^{4+} + 4OH^- \rightleftarrows U(OH)_4 \qquad k_1 = \frac{[U(OH)_4]}{[U^{4+}][OH^-]^4} \qquad (1)$$

$$U(OH)_{4-n}^{n+} + C_{18:1}E_9COO^- \rightleftarrows C_{18:1}E_9COOU(OH)_{4-n}^{(n-1)+} \qquad k_{2,n} = \frac{[C_{18:1}E_9COOU(OH)_{4-n}^{(n-1)+}]}{[U(OH)_{4-n}^{n+}][C_{18:1}E_9COO^-]} \qquad (2)$$

While at 25 °C, $\log k_1$ is known and comprised between 45 and 47 according to different studies[50-53], $\log k_{2,n}$ is unknown. However, the complexation constants of U(IV)

with others carboxylic acids can be found in the literature. For simple acids like acetic acid, based on Andra thermodynamic database[54], the complexation constant of $U^{4+}$ with acetate$^{-}$ is log k = 5.64 $\pm$ 1.00. For more complex acids such as α-isosaccharinic acid and gluconic acid, Warwick et al. reported a stability constants of U(IV) at 25 °C around $\log k_{2,1}$ = 50[55]. In case of $C_{16/18:1}E_9COOH$ surfactants, which present strong ion-complexing polar heads, the depolarization of alkyl chains may enhance the complexing ability and makes them stronger complexing agents comparable to complex acids[32, 56]. In that case, $\log k_1$ and $\log k_{2,1}$ should be close, explaining the distribution of U(IV) species as U- $C_{16/18:1}E_9COOH$ complexes and as nc-$UO_2$ ($U(OH_4)$ is not stable and directly forms $UO_2$(am) and then $UO_2$(cr)).

Consequently in this system, strong electrostatic interaction between U(IV) and $C_{16/18:1}E_9COOH$ surfactants in competition with U(IV) complexation by $OH^-$ avoids a fast nc-$UO_2$ formation and their uncontrolled aggregation.

## 4. CONCLUSION

A family of metastable colloidal sols of uranium using U(IV) as precursor and carboxylic surfactants ($C_{16/18:1}E_9COOH$ and $C_{12}E_{10}COOH$) has been successfully prepared by indirect precipitation for 6≤pH≤8 and molar ratio of U/S<0.3. The system consists of core-shell micelles, U(IV) species complexed by surfactant molecules forming multi-lamellar vesicles with interdigitated bilayers, nc-$UO_2$ within the vesicles and nc-$UO_2$ forming aggregates attached on the surface of the vesicles.

The competition between the U(IV) species complexation by surfactant molecules and their hydrolysis prevents the rapid condensation of $U(OH)_{4-n}^{n+}(1\leq n\leq 4)$ and makes the sol-gel process controllable.

Furthermore, this hierarchical structured colloidal system containing nanoparticles of 1 to 3 nm diameter as well as the bigger particles made from aggregated nanoparticles described here shows great interest for the nuclear fuel fabrication. The surfactant removal of this system would result in the packing of the nanoparticles of the system. This would lead to the formation of empty volumes between the nanoparticles from 0.3 to 3 nm diameter[57]. Such pores may be typically in the range of mesopores (2 to 50 nm[58]).

An ideal mixed oxide fuel for fast neutron reactors would be made by the filling of such mesoporous $UO_2$ with a $PuO_2$ concentrated solution. Thus, the problem of hot spot due to local density fluctuations of U/Pu ratio existing with the current nuclear fuel could be avoided.

## ACKNOWLEDGMENT

The authors thank Xavier Le Goff for his assistance in TEM experiments and data analysis, the LIME for the use of the facilities and Stéphanie Szenknect for the fruitful discussion. This work is a part of the PhD project of Zijie LU, which is financially supported by China Scholarship Council (CSC).

# REFERENCES

[1] A.R. Kaufmann, Nuclear Reactor Fuel Elements: Metallurgy and Fabrication, Interscience Publishers1962.
[2] S.-i. Hasegawa, E. Takano, M. Sekine, Process for manufacturing uranium dioxide powder, Google Patents, 1985.
[3] V.S. Yemel'Yanov, A.I. Yevstyukhin, The metallurgy of nuclear fuel: properties and principles of the technology of uranium, thorium and plutonium, Elsevier2013.
[4] T. Shiratori, K. Fukuda, Fabrication of very high density fuel pellets of thorium dioxide, J Nucl Mater, 202 (1993) 98-103.
[5] C.S. Caldwell, K.H. Puechl, PLUTONIUM--URANIUM DIOXIDE POWDER AND PELLET FUEL MANUFACTURE, Nuclear Materials and Equipment Corp., Apollo, Pa., 1968.
[6] S. Bataller, M. Ganivet, H. Guillet, Y. Masselot, A. Robillard, F. Stosskopf, MIXED URANIUM--PLUTONIUM OXIDE FUEL FABRICATION FOR RAPSODIE, CEA, Saclay, France, 1968.
[7] H.M. Mattys, PLUTONIUM METALLIC AND CERAMIC FUEL FABRICATION AND DEVELOPMENT AT THE EUROPEAN INSTITUTE FOR TRANSURANIUM ELEMENTS, EURATOM, Karlsruhe, Ger., 1968.
[8] R. Vauchy, A.C. Robisson, F. Audubert, F. Hodaj, Ceramic processing of uranium-plutonium mixed oxide fuels (U1-yPuy)O2 with high plutonium content, Ceram Int, 40 (2014) 10991-10999.
[9] G.W. Cunningham, United States Experience in Powder Metallurgy for Nuclear Applications, Powder Metall, 10 (1967) 78-93.
[10] V.N. Vaidya, Sol-gel process for ceramic nuclear fuels, Transactions of the Indian Ceramic Society, 63 (2004) 163-167.
[11] C. Ganguly, Sol-Gel Microsphere Pelletization: A Powder-Free Advanced Process for Fabrication of Ceramic Nuclear-Fuel Pellets, B Mater Sci, 16 (1993) 509-522.
[12] V.N. Vaidya, Status of sol–gel process for nuclear fuels, J Sol-Gel Sci Techn, 46 (2008) 369-381.
[13] D.D. Sood, The role sol–gel process for nuclear fuels-an overview, J Sol-Gel Sci Techn, 59 (2011) 404-416.
[14] M. Aparicio, A. Jitianu, L.C. Klein, Sol-gel processing for conventional and alternative energy, Springer Science & Business Media2012.
[15] C.L. Corkhill, D.J. Bailey, F.Y. Tocino, M.C. Stennett, J.A. Miller, J.L. Provis, K.P. Travis, N.C. Hyatt, Role of Microstructure and Surface Defects on the Dissolution Kinetics of CeO2, a UO2 Fuel Analogue, Acs Appl Mater Inter, 8 (2016) 10562-10571.
[16] J. Quiñones, E. Iglesias, A. Martínez-Esparza, J. Merino, E. Cera, J. Bruno, J. De Pablo, I. Casas, J. Giménez, F. Clarens, Modelling of the spent fuel dissolution rate evolution for repository conditions. Matrix Alteration Model results and sensitivity analysis, MRS Online Proceedings Library Archive, 932 (2006).
[17] N. Kumar, R.K. Sharma, V.R. Ganatra, S.K. Mukerjee, V.N. Vaidya, D.D. Sood, Studies of the Preparation of Thoria and Thoria-Urania Microspheres Using an Internal Gelation Process, Nucl Technol, 96 (1991) 169-177.
[18] V.N. Vaidya, S.K. Mukerjee, J.K. Joshi, R.V. Kamat, D.D. Sood, A Study of

Chemical-Parameters of the Internal Gelation Based Sol-Gel Process for Uranium-Dioxide, J Nucl Mater, 148 (1987) 324-331.
[19] P. Kovacheva, G. Avdeev, D. Todorovsky, Mechanochemically induced synthesis of UO2+x and uranium-thorium mixed oxides from sol-gel produced precursors, J Radioanal Nucl Ch, 287 (2011) 519-524.
[20] X.M. Fu, T.X. Liang, Y.P. Tang, Z.C. Xu, C.H. Tang, Preparation of UO2 kernel for HTR-10 fuel element, J Nucl Sci Technol, 41 (2004) 943-948.
[21] A. Deptula, M. Brykala, W. Lada, T. Olczak, D. Wawszczak, G. Modolo, H. Daniels, A.G. Chmielewski, Synthesis of uranium and thorium dioxides by Complex Sol-Gel Processes (CSGP).
[22] R. Zhao, L. Wang, Z.F. Chai, W.Q. Shi, Synthesis of ordered mesoporous uranium dioxide by a nanocasting route, Radiochim Acta, 104 (2016) 549-553.
[23] F. Schuth, Non-siliceous mesostructured and mesoporous materials, Chem Mater, 13 (2001) 3184-3195.
[24] D. Gu, F. Schuth, Synthesis of non-siliceous mesoporous oxides, Chem Soc Rev, 43 (2014) 313-344.
[25] C. Reitz, J. Haetge, C. Suchomski, T. Brezesinski, Facile and General Synthesis of Thermally Stable Ordered Mesoporous Rare-Earth Oxide Ceramic Thin Films with Uniform Mid-Size to Large-Size Pores and Strong Crystalline Texture, Chem Mater, 25 (2013) 4633-4642.
[26] W.G. Vandersluys, A.P. Sattelberger, Actinide Alkoxide Chemistry, Chem Rev, 90 (1990) 1027-1040.
[27] D.L. Clark, A.P. Sattelberger, W.G. Vandersluys, J.G. Watkin, New Development in Actinide Alkoxide Chemistry, J Alloy Compd, 180 (1992) 303-315.
[28] J.-P. Jolivet, M. Henry, J. Livage, Metal oxide chemistry and synthesis: from solution to solid state, Wiley-Blackwell2000.
[29] G.J.D. Soler-illia, C. Sanchez, B. Lebeau, J. Patarin, Chemical strategies to design textured materials: From microporous and mesoporous oxides to nanonetworks and hierarchical structures, Chem Rev, 102 (2002) 4093-4138.
[30] M. Leblanc, J. Causse, Z.J. Lu, D. Rebiscoul, Stable uranium sols as precursors for the elaboration of nanostructured nc-UO2 materials, Colloid Surface A, 522 (2017) 18-27.
[31] C. Micheau, P. Bauduin, O. Diat, S. Faure, Specific Salt and pH Effects on Foam Film of a pH Sensitive Surfactant, Langmuir, 29 (2013) 8472-8481.
[32] C. Micheau, Polyethoxylated carboxylic surfactant for ion foam flotation: fundamental study from solution to foam; Tensioactif carboxylique polyethoxyle pour la flottation ionique: etude fondamentale de la solution a la mousse, (2013).
[33] A. Saravia, Synthesis of carbide fuels from nano-structured precursors: impact on carbo-reduction and physico-chemical properties, France, 2015, pp. 218.
[34] N. Dacheux, V. Brandel, M. Genet, Synthesis and Properties of Uranium Chloride Phosphate Tetrahydrate - Uclpo4-Center-Dot-4h2o, New J Chem, 19 (1995) 1029-1036.
[35] N. Dacheux, V. Brandel, M. Genet, Synthesis and Characterization of Mixed-Valence Uranium Orthophosphate - U(Uo2)(Po4)(2), New J Chem, 19 (1995) 15-25.
[36] Y.H. Wang, M. Frutschi, E. Suvorova, V. Phrommavanh, M. Descostes, A.A.A. Osman, G. Geipel, R. Bernier-Latmani, Mobile uranium(IV)-bearing colloids in a mining-impacted

wetland, Nat Commun, 4 (2013).
[37] H.M. Wu, Y.G. Yang, Y.C. Cao, Synthesis of colloidal uranium-dioxide nanocrystals, J Am Chem Soc, 128 (2006) 16522-16523.
[38] G.I.N. Bouala, N. Clavier, R. Podor, J. Cambedouzou, A. Mesbah, H.P. Brau, J. Lechelle, N. Dacheux, Preparation and characterisation of uranium oxides with spherical shapes and hierarchical structures, Crystengcomm, 16 (2014) 6944-6954.
[39] P.D.F. Icdd, International Centre for Diffraction Data, Powder Diffraction File, Newtown Square, Pennsylvania, USA, (1997).
[40] C. Tanford, Micelle Shape and Size, J Phys Chem-Us, 76 (1972) 3020-&.
[41] S.A. Simon, T.J. Mcintosh, Interdigitated Hydrocarbon Chain Packing Causes the Biphasic Transition Behavior in Lipid Alcohol Suspensions, Biochim Biophys Acta, 773 (1984) 169-172.
[42] T.J. Mcintosh, R.V. Mcdaniel, S.A. Simon, Induction of an Interdigitated Gel Phase in Fully Hydrated Phosphatidylcholine Bilayers, Biochim Biophys Acta, 731 (1983) 109-114.
[43] J.X. Mou, J. Yang, C. Huang, Z.F. Shao, Alcohol Induces Interdigitated Domains in Unilamellar Phosphatidylcholine Bilayers, Biochemistry, 33 (1994) 9981-9985.
[44] J.N. Israelachvili, Intermolecular and surface forces, Academic press2011.
[45] G.A. Ferreira, W. Loh, Structural Parameters of Lamellar Phases Formed by the Self-Assembly of Dialkyldimethylammonium Bromides in Aqueous Solution, Journal of the Brazilian Chemical Society, 27 (2016) 392-401.
[46] J.H.K. Rozenfeld, E.L. Duarte, T.R. Oliveira, C. Lonez, J.M. Ruysschaert, M.T. Lamy, Oligonucleotide Adsorption Affects Phase Transition but Not Interdigitation of diC14-Amidine Bilayers, Langmuir, 29 (2013) 11102-11108.
[47] T.R. Oliveira, E.L. Duarte, M.T. Lamy, M. Vandenbranden, J.M. Ruysschaert, C. Lonez, Temperature-Dependence of Cationic Lipid Bilayer Intermixing: Possible Role of Interdigitation, Langmuir, 28 (2012) 4640-4647.
[48] L.W. Jia, C. Guo, L.R. Yang, J.F. Xiang, Y.L. Tang, C.Z. Liu, H.Z. Liu, Mechanism of PEO-PPO-PEO micellization in aqueous solutions studied by two-dimensional correlation FTIR spectroscopy, J Colloid Interf Sci, 345 (2010) 332-337.
[49] I. Breßler, J. Kohlbrecher, A.F. Thünemann, SASfit: a tool for small-angle scattering data analysis using a library of analytical expressions, Journal of applied crystallography, 48 (2015) 1587-1598.
[50] D. Rai, A.R. Felmy, S.M. Stemer, D.A. Moore, M.J. Mason, C.F. Novak, The solubility of Th (IV) and U (IV) hydrous oxides in concentrated NaCl and MgCl2 solutions, Radiochim Acta, 79 (1997) 239-248.
[51] D. Rai, A.R. Felmy, J.L. Ryan, Uranium (IV) hydrolysis constants and solubility product of UO2. cntdot. xH2O (am), Inorganic Chemistry, 29 (1990) 260-264.
[52] T. Yajima, Y. Kawamura, S. Ueta, Uranium(Iv) Solubility and Hydrolysis Constants under Reduced Conditions, Mater Res Soc Symp P, 353 (1995) 1137-1142.
[53] V. Neck, J.I. Kim, Solubility and hydrolysis of tetravalent actinides, Radiochim Acta, 89 (2001) 1-16.
[54] E. Giffaut, M. Grive, P. Blanc, P. Vieillard, E. Colas, H. Gailhanou, S. Gaboreau, N. Marty, B. Made, L. Duro, Andra thermodynamic database for performance assessment: ThermoChimie, Appl Geochem, 49 (2014) 225-236.
[55] P. Warwick, N. Evans, T. Hall, S. Vines, Stability constants of

uranium(IV)-alpha-isosaccharinic acid and gluconic acid complexes, Radiochim Acta, 92 (2004) 897-902.
[56] C. Micheau, O. Diat, P. Bauduin, Ion foam flotation of neodymium: From speciation to extraction, J Mol Liq, 253 (2018) 217-227.
[57] Z. Lu, D. Rébiscoul, J. Causse, X. le Goff, N. Mollard, X. Deschanels, Elaboration of microporous CeO 2 thin layers having nanocrystallites network controlled by Pluronic P123: Impact of key experimental parameters, Journal of Sol-Gel Science and Technology, (2019) 1-12.
[58] A.D. McNaught, A.D. McNaught, Compendium of chemical terminology, Blackwell Science Oxford1997.

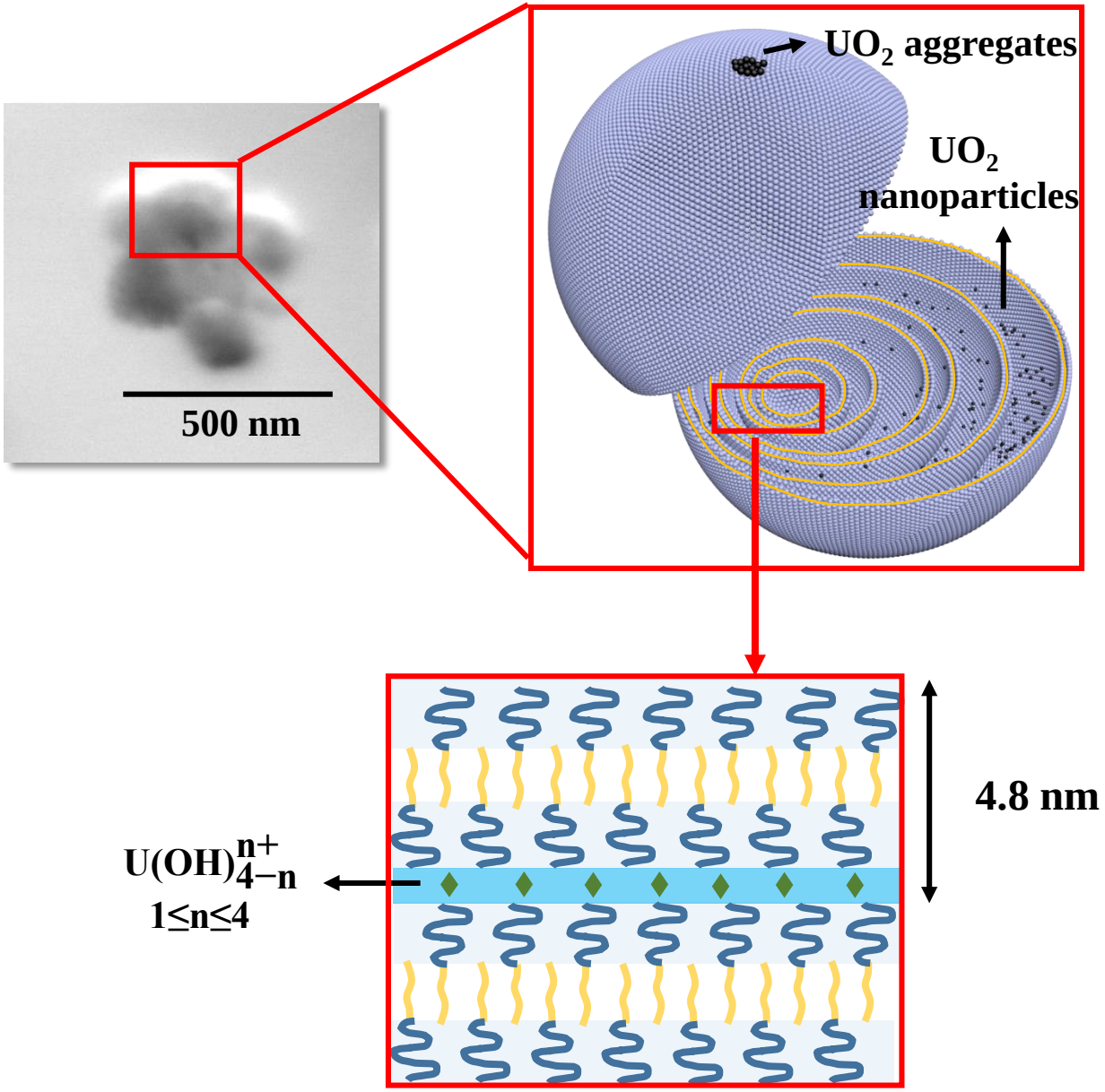
500 nm
$UO_2$ aggregates
$UO_2$ nanoparticles
$U(OH)_{4-n}^{n+}$
$1 \leq n \leq 4$
4.8 nm